JAMES | Journal of Advances in Modeling Earth Systems

RESEARCH ARTICLE
10.1029/2020MS002281

Mechanical Forcing of Convection by Cold Pools: Collisions and Energy Scaling

Bettina Meyer[1] and **Jan O. Haerter**[1,2,3]

[1]Niels Bohr Institute, University of Copenhagen, Copenhagen, Denmark, [2]Complexity and Climate, Leibniz Center for Tropical Marine Research, Bremen, Germany, [3]Physics and Earth Sciences, Jacobs University Bremen, Bremen, Germany

Key Points:
- A cold pool's initial potential energy is a good predictor of its spreading dynamics
- Cold pool radii evolve as a combinationof two power laws, highlighting a dynamic transition induced by "lobe-and-cleft" instabilities
- Updrafts and mass flux are strongly enhanced in multicold pool collisions compared to single cold pool gust fronts.

Correspondence to:
B. Meyer,
bettina.meyer@nbi.ku.dk

Citation:
Meyer, B., & Haerter, J. O. (2020). Mechanical forcing of convection by cold pools: Collisions and energy scaling. *Journal of Advances in Modeling Earth Systems*, *12*, e2020MS002281. https://doi.org/10.1029/2020MS002281

Received 7 AUG 2020
Accepted 19 OCT 2020
Accepted article online 26 OCT 2020

Abstract Forced mechanical lifting through cold pool gust fronts can trigger new convection and, as previous work highlights, is enhanced when cold pools collide. However, as shown by conceptual models, the organization of the convective cloud field emerging from two versus three colliding cold pools differs strongly. In idealized dry large-eddy simulations we therefore compare collisions between two and three cold pools. The triggering likelihood is quantified in terms of the cumulative vertical mass flux of boundary layer air and the instantaneous updraft strength, generated at the cold pool gust fronts. We find that cold pool expansion can be well described by initial potential energy alone. Cold pool expansion monotonically slows but shows an abrupt transition between an axisymmetric and a broken-symmetric state mirrored by a sudden drop in expansion speed. We characterize these two dynamic regimes by two distinct power law exponents and explain the transition by the onset of "lobe-and-cleft" instabilities at the cold pool head. Two-cold pool collisions produce the strongest instantaneous updrafts in the lower boundary layer, which we expect to be important in environments with strong convective inhibition. Three-cold pool collisions generate weaker but deeper updrafts and the strongest cumulative mass flux and are thus predicted to induce the largest midlevel moistening, which has been identified as a precursor for the transition from shallow to deep convection. Combined, our findings may help decipher the role of cold pools in spatially organizing convection and precipitation.

Plain Language Summary The arrival of a convective thunderstorm is often announced by strong and cold wind gusts that can be felt by an observer at the surface. These gust fronts constitute the outer edge of cold pools, which are formed underneath clouds when part of the rain reevaporates before reaching the surface, thereby cooling the air. These cold pools have received increasing attention due to their contribution in the generation of new convective rain events, thereby affecting the spatial pattern of the cloud field. In this study we use a high-resolution numerical model to study the life cycle of single cold pools and their collision with other cold pools. We assume that the likelihood that a cold pool causes a new rain event depends on (i) the vertical velocity of the wind gusts produced at its gust front and where it collides and (ii) how much moisture it can transport upward to a height where the water condenses and forms clouds. We show that both these factors are strongly increased where two or more cold pools collide, highlighting the importance of the representation of cold pool collisions in climate models to achieve a more realistic representation of clouds and rain.

1. Introduction

When rain re-evaporates in the boundary layer below a (deep) convection cloud (Droegemeier & Wilhelmson, 1985; Simpson, 1980), the evaporation locally cools the air beneath the cloud, resulting in a density increase (Markowski & Richardson, 2010). Gravity accelerates the dense air toward the surface, where it spreads horizontally as a gravity current. This spreading air mass is referred to as cold pool (CP). As laboratory and numerical investigations show, CPs can be seen as consisting of (i) a deeper head at the leading edge, ranging from a few hundred meters to several kilometers depth (Droegemeier & Wilhelmson, 1985), separated by a turbulent wake from (ii) a thin cold air "carpet" in the interior (Benjamin, 1968; Droegemeier & Wilhelmson, 1987; Kneller et al., 1999). The CP head characteristically is twice as deep as the interior (Markowski & Richardson, 2010; Simpson, 1972, 1980), containing most of the cold air and moisture from rain re-evaporation. A CP can further be characterized by its volume, propagation speed of the head, lifetime, and density, where density derives from both temperature and moisture anomalies. The CP's circulation can be decomposed into a shallow flow, directed radially away from the CP

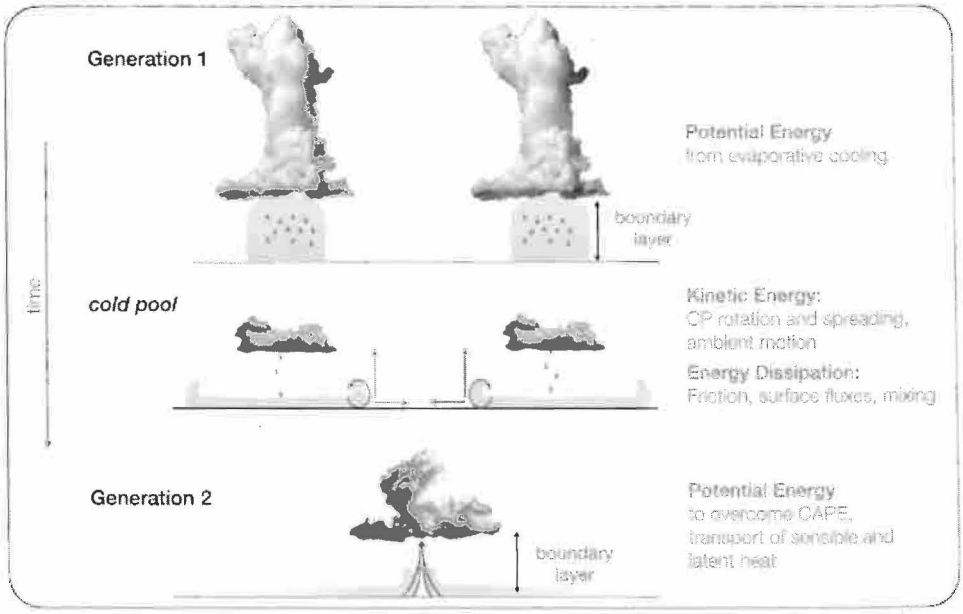

Figure 1. Simplified schematic of CPs linking convective events over space and time by converting the initial potential energy from evaporatively cooled air into kinetic energy of a CP, which by triggering convection transfers it back to potential energy of a second generation event.

center and causing the horizontal expansion of the CP, and a turbulent and rotational circulation within the CP head (Droegemeier & Wilhelmson, 1987; Cafaro & Rooney, 2018; Rotunno et al., 1988).

As a CP spreads along the surface, the radial density gradient and the radial motion create a narrow band of horizontal convergence of the near-surface wind field, which due to continuity causes pronounced updrafts in the atmospheric boundary layer aloft. These updrafts can lift the moist near-surface air to higher levels above the level of free convection (LFC) and moisten the upper boundary layer and lower troposphere, thereby triggering new convective events—an effect referred to as *mechanical* (or dynamical) forcing (Droegemeier & Wilhelmson, 1985; Purdom, 1976; Torri et al., 2015). In particular, under suppressed conditions with pronounced convective inhibition (CIN), this mechanical forcing may represent a major contribution to convection triggering. Especially in CPs over the ocean, the likelihood of convective triggering is further enhanced by an incremented moisture concentration in the CP head, referred to as *thermodynamic* forcing (Addis et al., 1984; Feng et al., 2015; Langhans & Romps, 2015; Tompkins, 2001a). Both the thermodynamic and mechanical effect are enhanced when CPs collide (Droegemeier & Wilhelmson, 1985; Feng et al., 2015), leading to increased likelihood of convection along lines or points where CPs collide, as found in observational and numerical studies (Feng et al., 2015; Kurowski et al., 2018; Torri & Kuang, 2019). Feng et al. (2015) found that the mean cloud fraction is increased by 70% along CP collision lines compared to single gust fronts. In this study, we quantify the enhancement of the mechanical forcing during CP collisions.

Enhancing convective triggering by carrying energy and moisture, CPs can be understood as a link between clouds across time and space (Figure 1): Rain from a Generation 1 convective cloud generates a CP, thereby moistening the air and transforming latent heat into potential and kinetic energy of the CP. Most of this energy and moisture (contributing to buoyancy) are contained in the CP head. As the CP spreads, energy and moisture are redistributed horizontally and vertically through lateral expansion and gust front dynamics. Thanks to this spatiotemporal link, CPs affect not only the cloud cover's local properties but also shape its mesoscale organization. Given an ensemble of Generation 1 convective cells and corresponding CPs, Generation 2 convective cells appear to be non-randomly connected to the present ones, leading to the emergence of complex, non-random, organizational patterns (Feng et al., 2015; Haerter

et al., 2019, 2020; Purdom, 1976; Torri & Kuang, 2019). Simple geometric models reveal that if the collision of any pair of two CPs yields a new convective cell, and thus a new CP, the number density of CPs inevitably increases and even diverges with time (Nissen & Haerter, 2020). Restricting such a model, conversely, to initiate new rain cells only where three distinct CP gust fronts collide, the population of CPs decreases over time —leading to a scale increase, when measuring typical distances between rain cells (Haerter et al., 2019). Hence, a better understanding of when and why two or three CPs are required for initiation of a new event is invaluable for properly capturing organization effects in climate models.

Apart from small fluctuations, in the atmospheric boundary layer the thermodynamic fields are vertically well mixed, while the vertical velocity can show pronounced turbulent structure. This implies that thermodynamic perturbations show less sensitivity to model resolution than the dynamic ones, as e.g. vertical velocity (Hirt et al., 2020), and can be reasonably captured at the kilometer scale of convection-resolving models (Leutwyler et al., 2016). Therefore, in this paper we focus on CP dynamics and the mechanical lifting. We do so by considering purely dry atmospheres in numerical high-resolution simulations, where CPs are characterized solely by a temperature anomaly, while moisture is neglected.

In such a dry setting, a CP's effectiveness of triggering new convection is determined by the strength of the circulation—updrafts and connected overturning circulation—it induces in its environment. This circulation is proportional to the CP's height and propagation velocity, where, according to a long line of numerical and conceptual studies, the latter can be related to the temperature anomaly and height of the CP (Benjamin, 1968; Grant & van den Heever, 2016; Moncrieff & So, 1989; Rooney, 2015, 2018). Thus, it is important to understand how the CP height and temperature anomaly scale with the size and strength of the initial rain event and evolve in time. In the simplest case, a steady-state solution is assumed, allowing to relate the CP's propagation speed to the density and height of the CP head, as an estimate of the CP's potential energy (Benjamin, 1968; Moncrieff & So, 1989). Such a situation can be generated by using a continuous forcing as in Droegemeier and Wilhelmson (1987), who studied the scaling in terms of the horizontal extent, height, and temperature of the initial cold air anomaly. However, in regards to modeling and prediction, it is beneficial to reduce the number of parameters and link the CP's properties directly to the strength and duration of a rain event. For this purpose, we here empirically derive a scaling of CP properties in terms of the potential energy of the one-time (i.e., discontinuous) initial cold air anomaly. We argue that despite the simplifications, these results can be used to understand how CP dynamics scales with the size and intensity of rain events.

We then study the triggering of convection events by CPs, focusing on whether new events are more often triggered at the gust front of a single CP or where multiple CP fronts collide. We examine this distinction from a dynamic perspective, assuming the likelihood of triggering new convection to monotonically increase with the strength and height of updrafts that are generated at the gust front of a single CP or at collision lines where multiple CPs meet, and the time-integrated mass flux at a given location. A similar argument has been used by Feng et al. (2015), who show that at locations where two or more CPs collide, updraft strength tends to be increased. The setup of the large-eddy simulations (LESs) is described in section 2. Results are presented in sections 3 and 4 for single and multi-CP effects and we end with a discussion (section 5), which relates the results to the more complex, moist convection in more realistic settings.

2. Large-Eddy Simulations

Simulation setup. The simulations are run using the LES code PyCLES (Pressel et al., 2015), which solves the anelastic equations for momentum and entropy using a dynamic time step. Sub-grid scale (SGS) diffusion is added using the Smagorinsky scheme (Smagorinsky, 1963). The resolution is isotropic with $\Delta x = \Delta y = \Delta z \in \{25,\ 50,\ 100\,\mathrm{m}\}$. Domain size is $L_z = 12$ km vertically for all simulations, while the horizontal size was varied from $L_{x,y} = 20$–40 km for the single CP simulations (sections 3.1 and 3.2), and from $L_{x,y} = 32$–80 km for the multi-CP simulations (*compare* Table C2). We employ periodic lateral boundary conditions. Turbulent fluctuations are initialized by adding weak noise in potential temperature θ of amplitude $\theta' = 0.05$ K in all levels below $z = z^* + 2 \cdot \Delta z$, where z^* is the height of the initial cold air anomaly. No surface heat and momentum fluxes are applied.

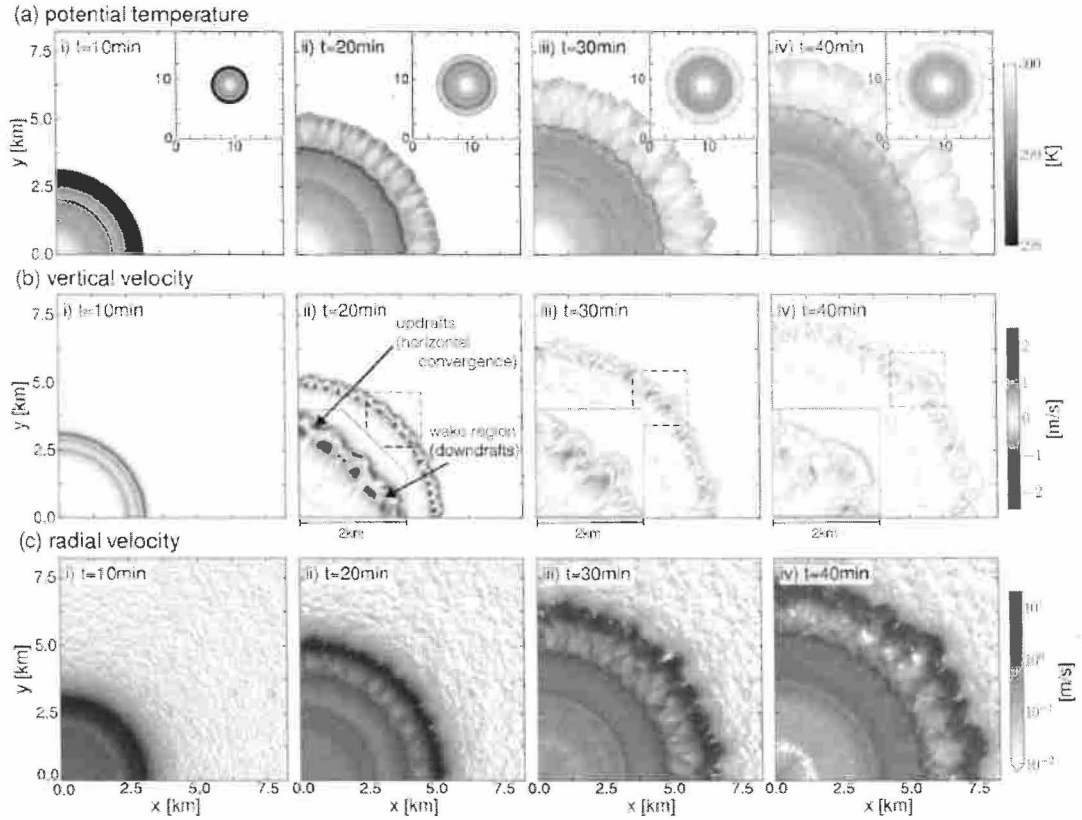

Figure 2. Internal cold pool structure. Horizontal cross sections of temperature and velocity in the lowest model level at various times after initialization (*see* the labels within the panels). The temperature anomaly was initialized as $\theta' = -3$ K and the geometry parameters $r^* = z^* = 1$ km ($\Delta x = 25$ m, $L_{x,y} = 20$ km). (a) potential temperature; (b) vertical velocity showing updrafts (red) and downdrafts (blue), which due to continuity corresponds to the convergenceof the horizontal velocity; and (c) radial velocity. Insets in (a) show an overview of the total CP. Insets in (b) show magnifications of the respective areas within the dashed boxes.

2.1. Cold Pool Initialization

The CPs are initialized by an initial mountain of cold air of height z^* and circular base of radius r^* at the lowest level (Equation A.1 and Figure A1). To reduce numerical errors, a transition layer of thickness $\delta = 200$ m is applied, in which the temperature anomaly smoothly decreases from $\theta = \theta_0 + \theta'$ to $\theta = \theta_0$. The temperature anomalies θ' are chosen commensurate with observations of deep tropical convection over the ocean, with -2 to -5 K (Feng et al., 2015; Johnson & Nicholls, 1983; Parsons et al., 1994; Zuidema et al., 2017), where CPs are weaker than in (organized) continental convection. The reference to CPs over the tropical ocean is motivated by the focus on CPs in a calm environment (*compare:* section 2.2) over flat topography—while for CPs over continents, the existence of environmental wind shear often crucially shapes their properties and role in convection triggering (Moncrieff & Liu, 1999; Rotunno et al., 1988). Furthermore, in the subsaturated boundary layer—which this study is focused on—we assume that it makes a minor difference whether this density anomaly is created by temperature or moisture, or both.

2.2. Surrounding Environment

Neutral stratification. The CPs spread into a calm, neutrally stratified environment with $\theta_0 = 300$ K (Figure 2), where all velocities are initially set to zero. No surface fluxes are applied, leading to extended CP life times due to decreased dissipation near the surface. As motivated by Droegemeier and Wilhelmson (1987), such a highly idealized setup allows to isolate the effects of CPs on the environment without the obscuring effects from wind shear and gravity waves or the collision with existing circulation

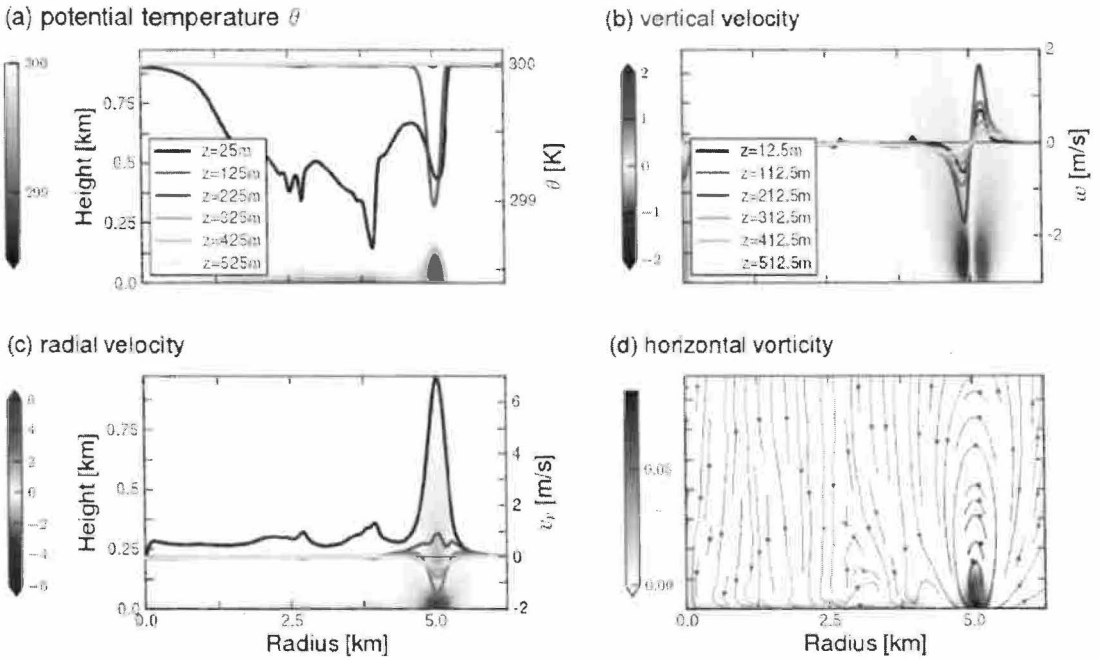

Figure 3. Thermodynamic and dynamic signature of a spreading cold pool. (a) $z - r$ contour plot and cross sections of azimuthally averaged potential temperature θ, where the cross sections show increasing levels of z (*see* legend) 20 min after CP initialization (LES parameters analogous to Figure 2). (b) Analogous to (a), but for vertical velocity w; (c) analogous to (a), but for radial velocity v_r; (d) similar, but showing vorticity projected onto the radial vector (units of s^{-1}, with superimposed streamlines of v_r and w.

patterns from previous convection events. To test the results of the CP collisions in a more realistic environment, an additional set of experiments is conducted in a stably stratified atmosphere.

Stable stratification. Atmospheric soundings usually show a stable stratification above the boundary layer top. To test the effect of stratification on the updrafts generated at CP gust fronts and during CP collisions, we compare simulations with neutral and weakly stable stratifications at $z > 1{,}000$ m, adopting the conditions used in Grant and van den Heever (2018) to a dry atmosphere. The stable case is characterized by a constant Brunt-Väisälä frequency of $N_v^2 = \frac{g}{\theta}\frac{\partial\theta}{\partial z} = 5 \cdot 10^{-5}\ s^{-2}$. This induces gravity waves atop the CP center at an oscillation period of $\tau = N_v^{-1} \approx 140$ s.

2.3. Cold Pool Collisions

To study CP collisions, the simulations are initialized with two or three identical CPs, with CP centers separated by a distance $d = 10$, 15, and 20 km. In the three-CP collision, d corresponds to the side length of the equilateral triangle with CPs initialized at all three corners (Figure 6). The values of d are in line with typical distances between the centers of convective events in radiative-convective equilibrium simulations (Nissen & Haerter, 2020).

3. Results Single Cold Pool

3.1. Cold Pool structure

After initialization, the cold air "mountain" collapses and spreads isotropically along the surface, forming the CP (Figure 2). During the first 10–15 min, the CP retains its almost perfect circular symmetry, where deviations from the azimuthal mean are small both in the temperature and velocity fields (Figure 2, column i). During the collapse of the cold air "mountain," the horizontal temperature gradient induces baroclinic generation of a vortex sheet along the lateral boundary of the temperature anomaly, which finally

rolls up into a vortex ring that forms the clearly visible CP head (Figure 3d) (Droegemeier & Wilhelmson, 1987; Moncrieff & So, 1989; Markowski & Richardson, 2010; Rooney, 2018). While spreading, the CP head becomes fairly detached from the shallow CP interior and maintains a colder and deeper temperature anomaly (Figure 3a).

The vortical circulation leads to a dipole structure in vertical velocity w with strong updrafts ahead of and downdrafts behind the CP head in the wake (Figures 2b and 3b). In this downdraft region warm environmental air is entrained into the CP head, boosting the CP's dissipation. Ahead of the CP head, the vortex ring and the spreading of the CP form a band of convergence of the horizontal velocity (Figures 2c and 3c). The profiles of temperature and velocity (Figures 3a–3c) compare well to previous numerical studies, both in idealized (Droegemeier & Wilhelmson, 1987; Romps & Jeevanjee, 2016) and more comprehensive setups (Drager & van den Heever, 2017; Fournier & Haerter, 2019). The main difference to the latter studies is that the CP head there is less detached from the CP interior due to the more continuous forcing from rain events with a finite life time.

At a more mature stage, the vortex ring develops along-front instabilities that break the symmetry of the vortex ring (CP head) by dividing it into smaller cells typically measuring $500 - 1000m$ in diameter (Figure 2, insets). These so-called "lobe-and-cleft" instabilities occur as the CP head overruns lighter air that is trapped near the surface, leading to hydrodynamic linear instabilities that have been studied both in theory and laboratory experiments of gravity currents (Härtel et al., 2000; Markowski & Richardson, 2010; Simpson, 1972; Wakimoto, 2001). These instabilities can lead to the collapse and reformation of the CP head, leading to multi-ring structure near the surface (Figures 2 and 3; Goff, 1975). These small-scale features are highly sensitive to numerical resolution and in our simulations are only visible for $\Delta x \leq 50$ m. As shown in section 3.2, these instabilities have a crucial effect on the spreading velocity of the CP (Figure 5). It remains an open question, to which extent "lobe-and-cleft" instabilities play a role in observations and comprehensive cloud-resolving simulations, where CPs also spread into the environment not as a homogeneous front, but by protruding edges. In the interior of these edges (lobes), a circulation tangential to the CP front develops, which is reflected in an increased tangential velocity component of alternating direction. This breaks the symmetry into an periodic pattern of positive and negative horizontal convergence corresponding to updrafts and downdrafts aloft (Figure 2b, iii), where the triggering of new convective events may be enhanced.

Since we are interested in the dynamic forcing by CPs, namely, the location and strength of generated updrafts, we define the *CP radius R* as the distance between the CP center ($r = 0$) and the location of the maximum low-level convergence of horizontal wind

$$R = \max_{r}(\vec{\nabla}_h \cdot \vec{v}_h), \tag{1}$$

which is colocated with the maximum of the vertical updrafts $\max_r(w(r, \phi))$. This radius R and the corresponding propagation speed of the CP, $U \equiv dR/dt$, are determined using a tracer method introduced in Henneberg et al. (2020). The CPs spread to radii of approximately 10 km within an hour, which is in line with other numerical and observational studies (Feng et al., 2015; Romps & Jeevanjee, 2016; Tompkins, 2001b). Due to the vortical circulation in the CP head this method only allows to define the CP boundary at the lowest model levels ($z \leq 200$–300 m). At higher levels, the radial velocity becomes weaker until it reverses direction at the upper boundary of the CP head, resulting in weaker and more noisy horizontal convergence. For this reason, we define the *CP height* based on the thermodynamic signature, determining for each column the highest level where the potential temperature deviates by more than a small threshold from the background temperature $\theta_0(z)$:

$$H(x, y) = \max_{z}(|\theta_{CP}(x, y, z) - \theta_0(z)| < \epsilon). \tag{2}$$

Such a simple method is found sufficient in this idealized setup where the temperature is very homogeneous in the environment.

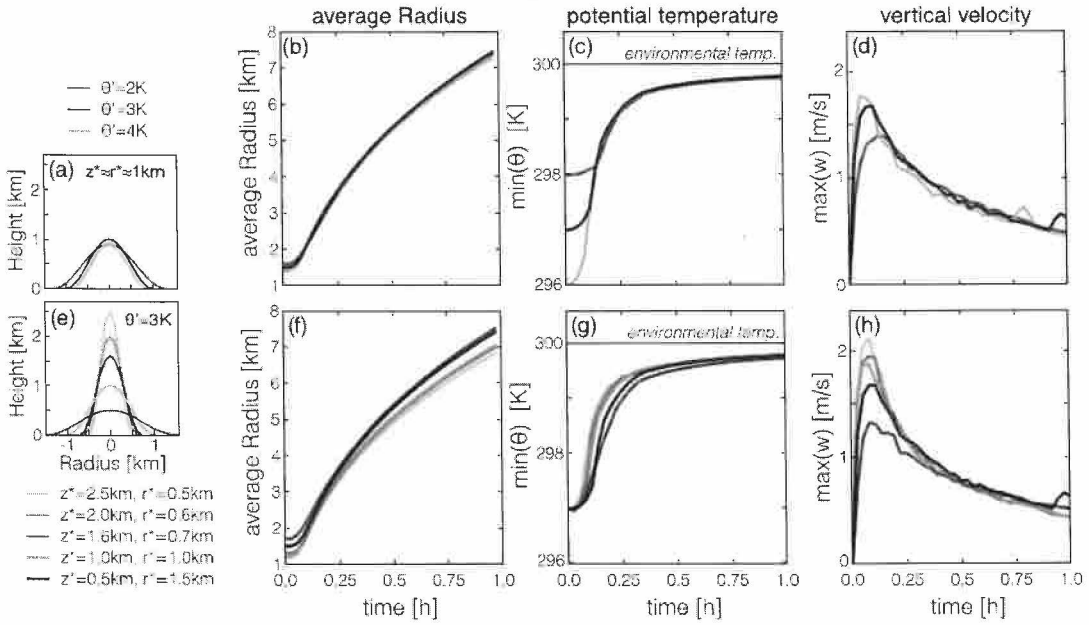

Figure 4. Time series of CP properties when holding potential energy fixed. (a) Schematic of CP geometry and temperature, when systematically modifying the temperature anomaly $\theta' \in \{-2, -3, -4\}$ K (as shown in the legend), but approximately maintaining the geometry parameters (r^*, z^*) = {(1.3 km, 0.9 km), (1.0 km, 1.0 km), (0.9 km, 0.9 km)} ($\Delta x = 50$ m, $L_{x,y} = 20$ km), (b) azimuthally averaged CP radius versus time after initiation, (c) analogous, but for domain minimum potential temperature, (d) analogous, but for maximum vertical velocity in the updrafts ahead of the CP, (e) analogous to panel a, but now systematically varying the ratio of z^* and r^* (modifying the geometry, see legend) at fixed $\theta' = 3$ K, again maintaining $PE = PE_0$. (f-h) analogous to panels (b)–(d), but for the initial conditions shown in panel (e).

3.2. Scaling of Cold Pool Properties With Initial Potential Energy

This section considers the hypothesis that key CP properties, such as CP propagation speed and the strength of the generated updrafts at the CP gust front, are insensitive to the exact shape and temperature anomaly of the initial configuration but are solely determined by the initial potential energy (termed PE). This notion builds on early theoretical studies by Benjamin (1968) and Rotunno et al. (1988) and adds detail to the sensitivity study on outflow morphology and structure by Droegemeier and Wilhelmson (1987), by showing that the parameter space of at least three variables (magnitude, depth and vertical shape of the cooled volume) can be collapsed to a single dimension—namely, that of PE—a quantity that can be studied in the context of energy budgets.

In our simple dry setup with neutral background stratification, PE depends on the initial temperature anomaly θ' and the volume of the initial mountain—in turn a function of the geometry parameters for the height and radius of the anomaly, termed z^* and r^*, respectively. As an integral over the specified volume (Equation A1), PE can be computed as

$$PE = g \int \mathrm{d}V \frac{\theta'(\vec{x})}{\theta_0(z)} \rho_d(z) \cdot z \approx g \frac{\theta'}{\theta_0} \rho_0 \int \mathrm{d}V z \propto \theta' (r^* z^*)^2, \tag{3}$$

where $\rho_d(z) \approx \rho_0 \approx 1\,\mathrm{kg\,m^{-3}}$ is the density of dry air in the CP's environment (*compare* Appendix A for details).

First, we run experiments where PE is held constant at a reference value $\mathrm{PE}_0 \approx 4.4 \cdot 10^7$ kJ, whereas r^*, z^* and the initial temperature anomaly θ' are varied. PE_0 corresponds to a CP with initial temperature anomaly $\theta_0' = 3K$ and $r_0^* = z_0^* = 1$ km. These experiments allow us to test whether the initial geometry of the CP

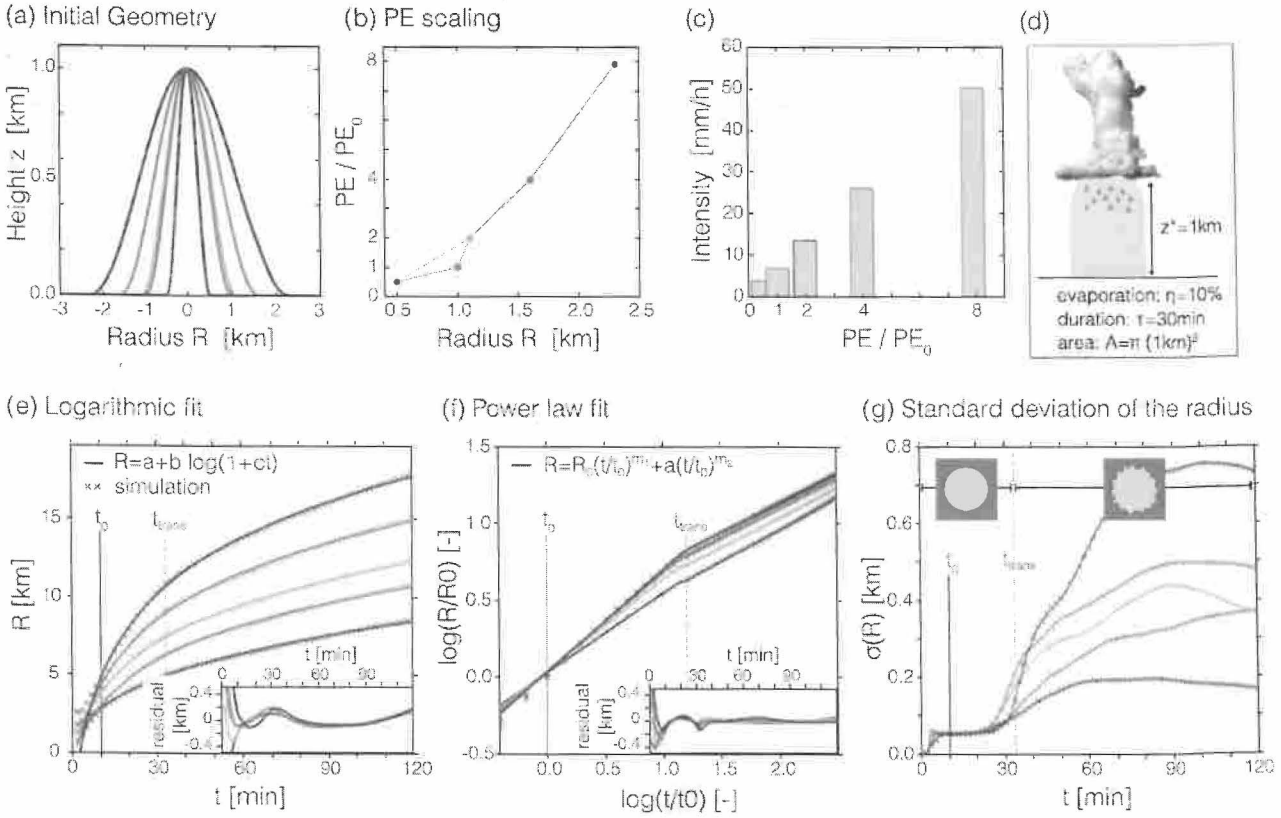

Figure 5. Scaling of cold pool radius with potential energy. (a and b) Initial geometry and corresponding PE. Symbol colors in (b) correspond to those of the different shapes in (a) ($r^* \in \{.5,\ 1.1,\ 1.6,\ 2.3\ \text{km}\}$, $z^* = 1.0$ km; $\Delta x = 50$ m, $L_{x,y} = 40$ km); (c) the relation of PE to precipitation intensity under simplifying assumptions; (d) schematic and values of underlying assumptions for (c); (e) Time series of the CP radius R for increasing PE (configurations as in a) ("×" symbols). Solid lines are logarithmic fits using $R = a + b\log(1 + ct)$ (Romps & Jeevanjee, 2016), and the solid and dashed vertical black lines indicate t_0, to define $R_0 = r(t = t_0)$, and t_{trans}; (f) Log-log plot of R versus t ("×" symbols) with best fits for power law scaling from Equation 5 (solid lines); (g) Time series of the standard deviation $\sigma(R)$ of the tracer radius, showing the transition from the axisymmetric CP state (small, approx. constant $\sigma(R)$) to the mature CP whose head is dominated by "lobe-and-cleft" instabilities (*compare*: Figure 2). The initial kink in $\sigma(R)$ near $t \approx 0$ is due to the initialization of the tracer particles at equal initial R—used for the tracking of the gust front. Note that $\log(x)$ denotes the natural logarithm.

impacts on its dynamics. Second, PE is varied, and the resulting scaling of CP properties studied—mimicking changes in precipitation intensity and resulting CP strength. Such intensity changes can occur within the diurnal cycle of precipitation, where intensifying precipitation cells might release increasingly more energy (Haerter et al., 2017, 2020).

Sensitivity to geometry and temperature anomaly. First, the temperature anomaly is varied as $\theta' \in \{-2, -3, -4\}$ K, whereas the geometry is adjusted only as much as is necessary to keep the PE constant (Figures 4a–4d). Second, $\theta' = -3K$ is held constant whereas the geometry is varied from a narrow and tall to a broad and shallow mountain (Figures 4e–4h).

The resulting CPs show very similar properties during their life cycles. The time series in Figure 4 represent the mean, minimum, or maximum values of azimuthally averaged quantities: the average radius R (Equation 1); the minimum potential temperature as a measure of CP dissipation, defined as $\theta_{\min}(t) = \min_{r,z}\left[1/(2\pi)\int d\phi\,\theta(r, \phi, z; t)\right]$; and the maximum vertical velocity $w_{\max}(t) = \max_{r,z}\left[1/(2\pi)\int d\phi\, w(r, \phi, z; t)\right]$. It has been verified that the points of minimum potential temperature and maximum vertical velocity are

Table 1
Fitting Parameters and Errors for the Mean CP Radius as a Function of Time and Initial Potential Energy

Logarithmic fit	r^* (km)	δR (m)	R_0 (m)	**b** (m)	**c** (10^{-3} s^{-1})	
$R(t) = a + b\log(1 + ct)$	0.5	8.0	2,835.0	3,573.0	0.6	
	1.0	7.9	2,971.0	3,871.0	1.0	
	1.1	12.0	3,803.0	4,248.0	0.9	
	1.6	12.2	4,272.0	5,084.0	1.1	
	2.3	10.5	4,699.0	5,811.0	1.3	
Power law fit	r^* (km)	δR (m)	$\log a_1$ (-)	m_1 (-)	$\log a_2$ (-)	m_2 (-)
$R(t)/R_0 = a_i(t/t_0)^{m_i}$	.5	3.5	0.0	0.52	0.1	0.42
$i = 1$, for $t < t_{trans}$	1.0	3.3	0.0	0.64	0.3	0.41
$i = 2$, for $t \geq t_{trans}$	1.1	5.0	0.0	0.59	0.3	0.39
	1.6	5.0	0.0	0.64	0.3	0.39
	2.3	5.4	0.0	0.67	0.4	0.38

Note. Here, $t \in \{t_0, t_0 + 100, \ldots, 7\,100\}$ s, with the spin-up time $t_0 = 10$ min and $n_t = 65$ the total number of time steps. The transition time is chosen at $t_{trans} = 2000$ s. The mean square root error is computed as $\delta R = \frac{1}{n_t}\sqrt{\sum_{i=1}^{n_t}(\hat{R}_i - R_i)^2}$, where $\hat{R}_i = \hat{R}(t_i)$ is the estimated radius (from power law or logarithmic fit, respectively) and $R_i = R(t_i)$ the measured CP mean radius at time t_i.

measured within or in near proximity ahead of the CP head, respectively. The time series differ mostly at the initial formation of the density current ($t \leq 15$ min) but converge soon thereafter. Hence, after a spin-up time between initialization and density current formation, the simulations are rather insensitive to the geometry and temperature anomaly of the initial configuration and are largely determined by the initial PE.

Scaling with initial potential energy. All CPs are now initialized by $\hat{\theta}' = -5$ K and $z^* = 1$ km, whereas r^* is varied to scale the CPs' initial PE (Figures 5a and 5b). Resolution is $\Delta x = 50$ m and domain size is $L_{x,y} = 40$ km. If one thinks of the cooling as generated by rain of varying intensity that evaporates uniformly at an evaporation rate of $\eta = 20\%$ (Worden et al., 2007) during $\tau = 30$ min within the subcloud air column of height $z^* = 1$ km below a rain cell of horizontal area $A = \pi(1\,\mathrm{km})^2 \approx 3$ km^2 (Figure 5d), the range of PE values corresponds to rain intensities shown in Figure 5c (*compare:* calculation in Appendix B).

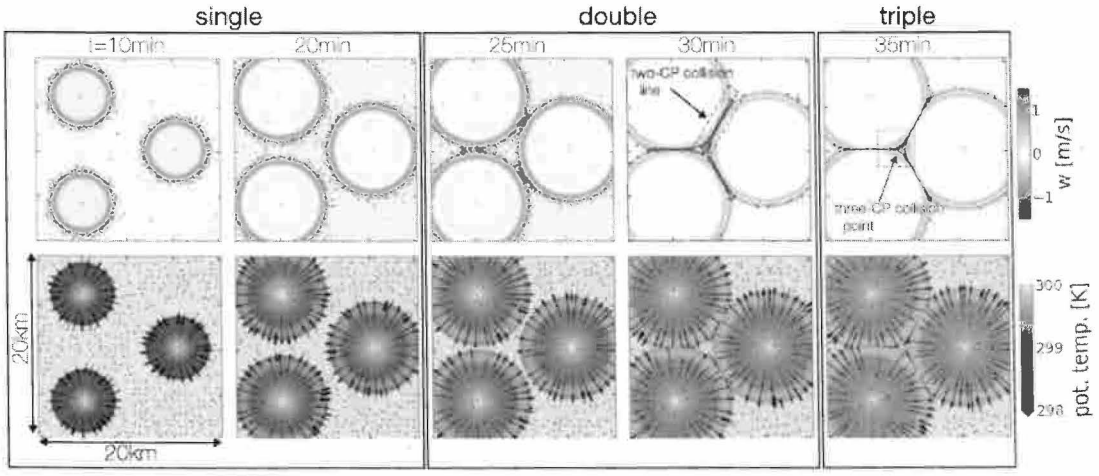

Figure 6. Simulated three-CP collisions. (top row) Vertical velocity at the lowest model level, $w(z = 50\,\mathrm{m})$, with contours depicting vertical velocity at a higher level ($w(z = 550$ m$) = 0.5$ m/s) indicating the updrafts triggered in the CP collisions (fluctuations at early times are forced by the initial temperature perturbations). Boxes indicate the confined locations where two and three CPs collide. (bottom) Potential temperature with streamlines of the horizontal wind field, both at the lowest model level ($z = 25\,\mathrm{m}$). Data from *3CP* simulation with $d = 12\,\mathrm{km}$ at $t = 10$, 20, 25, 30, and 35 min.

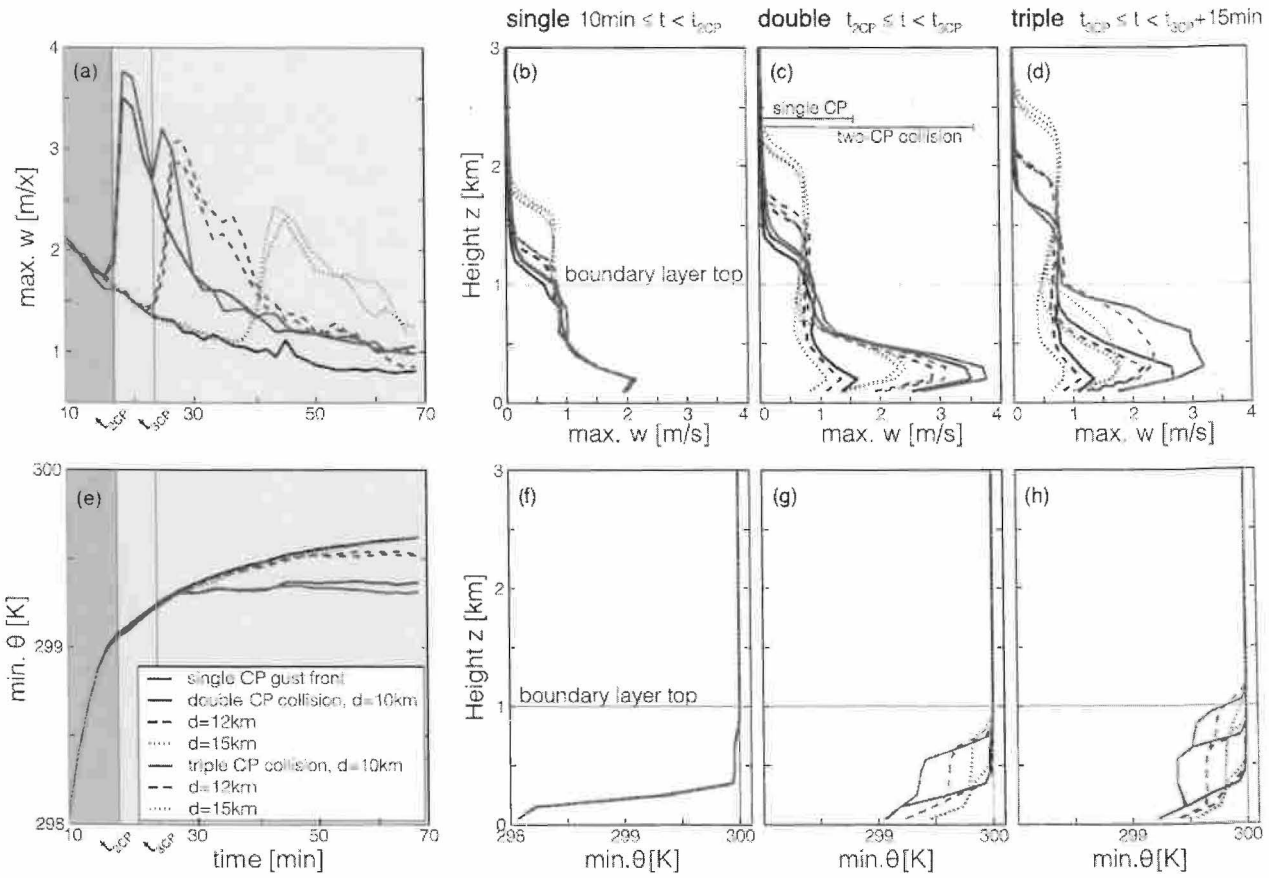

Figure 7. Updraft speed and CP height in collisions. (a) Time series of domain maximum values of vertical velocity w for the *1CP* (black), *2CP* (blue), and *3CP* (red) simulations with neutral background stratification ($\Delta x = 100$ m). Line styles indicate different initial CP separation of $d = 10$ km (solid line), 12 km (dashed line), and 15 km (dotted line); background color shadings refer to the time windows of undisturbed CPs (gray), two-CP collision (light blue) and three-CP collision (light red) for the shortest separation distance ($d = 10$ km). (b–d) Maximum values of vertical velocity w at each model level during the time window of (b) the single CP spreading, (c) two-CP collision, and (d) three-CP collision; (e–h) analogous to (a)–(d), but for minimum values of potential temperatur θ.

For all initial values of potential energy, CP expansion monotonically slows down, which has been described in previous studies. Romps and Jeevanjee (2016) approximated the decrease by a logarithmic dependence of radius on time, that is,

$$R(t) = R_0 + b\log(1 + c(t - t_0)). \tag{4}$$

Fitting the three parameters R_0, b, c to our simulation data indeed yields a visually acceptable fit within the time range considered (Figure 5e). However, the parameters vary substantially with PE(r^*) (*compare:* Table 1), and when examining the residuals (Figure 5e, inset), systematic oscillations are visible for all cases. When plotting the data using double-logarithmic axis scaling (Figure 5f), it becomes clear, that a transition between two power laws, each of the form

$$R(t)/\tilde{R} = (t/\tilde{t})^m, \quad \text{with} \tilde{R} = R(\tilde{t}), \tag{5}$$

but with a change in exponent m at a time t_{trans}, may also be appropriate and represents a more universal scaling law. The reference value $\tilde{R}$ is thereby a function of PE, following $\tilde{R}(\text{PE}) = R(\tilde{t}, \text{PE})$, and $\tilde{t} \in \{t_0, t_{\text{trans}}\}$.

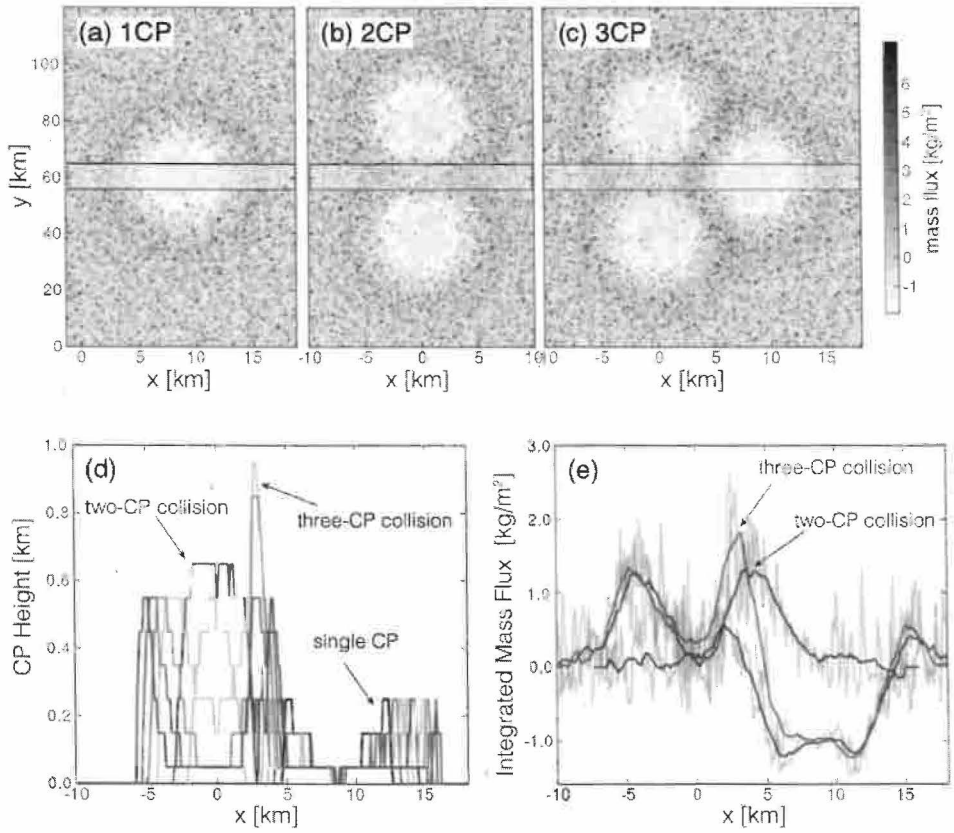

Figure 8. Cold pool height and accumulated vertical mass flux (MF). (a) Horizontal cross section of the accumulated vertical mass flux at$z = 1$ km for *1CP*, integrated from$t = 10$ min after initialization to $t_{3CP}+10$ min. The yellow box indicates the band of width 2 km along which *MF* is averaged in (e); (b and c) as in (a), but for the *2CP* and *3CP* simulations ($d = 10$ km). The same integration time window is used for each simulation, to ensure meaningful comparison. (d) Cross sections of the CP height in *3CP* along the box indicated in (c) at subsequent time instances (every 100 s from 800–1,600 s): during the single CP phase (gray to black), two-CP phase ($t_0 \le t < t_{2CP}$; light to dark blue), and three-CP phase ($t_{2CP} \le t < t_{3CP}$; light to dark red). (e) Accumulated mass flux at $z = 1$ km, spatially averaged over a band of 2 km width along the CP collision line, as indicated by the yellow shaded box in (a)–(c) from *1CP* simulation (black), *2CP* simulation (blue), and *3CP* simulation (red).

The spin-up time $t_0 = 10$ min is chosen as the time when the CP radii start following a systematic increase (Figures 4b and 4f).

The discontinuous slope in the log-log plot (Figure 5f) hence indicates a separation of the CP lifecycle into two dynamical regimes between which the power law exponent m changes. The transition occurs near $t_{trans} \approx 30$ min, and we attribute it to a dynamical transition from an axisymmetric state to one where "lobe-and-cleft" instabilities dominate the CP head (*compare*: Figure 2). This interpretation is verified by the standard deviation of the CP radius, which experiences a strong increase around the transition time (Figure 5g). For all simulations, this transition occurs at a similar time between 20 and 35 min, the exact time instance however does not follow a clear systematic dependence on PE. The monotonic increase of variance after the transition time suggests that the size of the lobe-cleft pattern scales with the CP radius.

The two scaling functions (Equations 4 and 5) are compared in terms of their "goodness of fit," considering the number of parameters, root-mean-square (RMS) deviation δR and their physical explanatory power, that is, how well they allow to separate the dependence on time from the dependence on PE. If for the power law fit

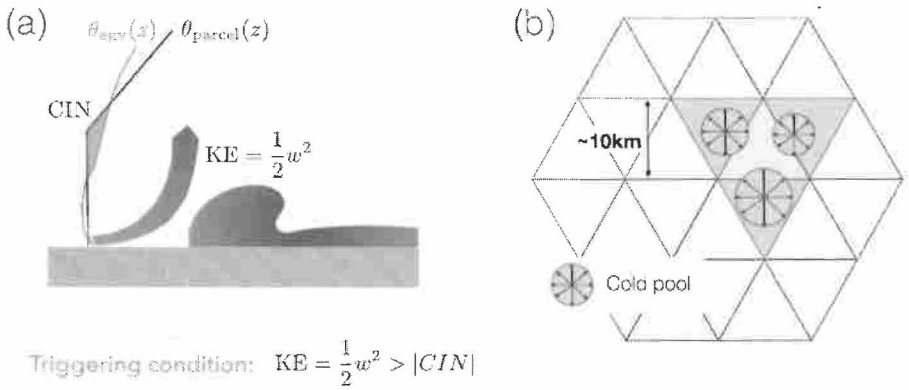

Figure 9. Cold pool parameterization. (a) The kinetic energy (KE) generated by cold pools allows updrafts to overcome a given convective inhibition (CIN) layer capping the boundary layer (adapted from Grandpeix & Lafore, 2010). (b) Role of cold pool collisions and nearest neighbor interaction in convection parameterization schemes for cloud-resolving models.

$$R(t)/R_0 = a_i (t/t_0)^{m_i}, \quad i = 1 \text{ for } t_0 \le t < t_{\text{trans}}, \quad i = 2 \text{ for } t \ge t_{\text{trans}},$$

a fixed transition time t_{trans} is chosen and R is rescaled by a fixed transition time t_{trans} is chosen and R is rescaled by $R_0 = R(t_0)$, the axis intercept a_1 becomes 1 (Table 1). Thus both fitted functions, logarithmic and power law, are determined by three parameters, which renders a comparison with respect to fitting errors valid. The power law fit outperforms the logarithmic fit both in terms of smaller systematic error (compare: Figures 5d and 5e insets) and smaller RMS δR (Table 1). Finally, for the logarithmic scaling, the optimal fitting parameters differ quite strongly for varying PE, whereas the power law exponents are approximately constant (Table 1): $m_1 \approx 0.5$–0.6, $m_2 \approx 0.4$. This gives the power law fit a more universal character. The magnitude of the residual from the power law fit is slightly sensitive to the choice of t_0, however, qualitatively, the comparison between the two fittings and the residual time series is robust, specifically when considering long time series that stretch beyond one hour of simulation time, where the RMS error for the logarithmic fit becomes approximately three times larger than that for the power law fit.

4. Results Cold Pool Collisions

To simulate the collisions, we initialize two (*2CP*) or three (*3CP*) identical CPs separated by distances of $d = 10$, 12, and 15 km (section 2). The updrafts generated and the corresponding mass fluxes are compared to an otherwise identical single CP (*1CP*) which spreads unrestrictedly. All CPs are initialized with $\theta' = 5K, z^* = 1$ km, and $r^* = 1.1$ km. The simulations run at resolution of $\Delta x = 100$ m, in domains of $L_{x,y} = 32$–80 km (*compare* Table C2).

Notably, the CPs have a very short "communication distance"; that is, they affect their environment and other CPs only within a very short distance beyond their leading edge, as is apparent from the very weak horizontal and vertical velocities outside the temperature anomaly (Figure 6). We thus define a CP collision as the instance when the CPs' gust fronts touch, defining the times of 2-CP collision ($t_{2\text{CP}}$) and 3-CP collision ($t_{3\text{CP}}$) (numerical values listed in Table C1). The collisions are delayed by approximately 10 min when d is increased by 5 km, indicating that the CPs spread at an average speed of 8 m/s.

Updraft generation. Figure 7 shows the maximum values of vertical velocity w (upper row) and minimum values of potential temperature (lower row) in the total domain (Figures 7a and 7e) and at each model level (Figures 7b-d and 7f-h). For $t_0 \le t < t_{2\text{CP}}$ (for $d = 10$ km corresponding to the first 18 min), the CPs of the multi-CP simulations (*2CP*, *3CP*) do not measurably affect each other. This results in equivalent CP properties for all simulations *1CP*, *2CP*, *3CP*, and all separation distances d (Figures 7b and 7f). The strongest updrafts are generated immediately ahead of the CP head, extending up to a height of roughly 1,000 m, with

strongest vertical velocities ($w \approx 2$ m/s) at the lowest model levels (100–300 m). The strength of these updrafts remains roughly constant while the CPs spread.

When the CPs collide in pairs of two ($t = t_{2CP}$), they form collision interfaces, along which the ambient air is displaced both vertically and horizontally as the flow is constrained to these two degrees of freedom. This creates updrafts that are both faster and reach greater heights: the vertical velocity is strongly increased in the lower boundary layer ($z < 600$ m) (Figures 6 and 7c) and the CP height is nearly doubled to $H_{max} \approx 700$ −800 m (Figure 7g). Notably, the maximum velocity for *2CP* is more than twice as large as for *1CP*. This factor indicates that the updrafts generated in CP collisions cannot simply be described as superpositions of the single CP updrafts and that horizontal kinetic energy may be transformed into vertical motion during the collisions. This nonlinearity may be enhanced by the superposition of the vortical circulation in the two CP heads (Cafaro & Rooney, 2018).

As the CPs continue to spread, the collision lines grow until in *3CP* they eventually meet at the center of the domain, forming a three-CP collision ($t = t_{3CP}$). The warm ambient air, enclosed by the CPs, as well as the colder CP air is then forced upward by the low-level convergence. The vertical velocity peaks in a locally very confined area around the collision point (Figure 6 at $t = 35$ min). This three-CP collision generates enhanced vertical velocities in the middle boundary layer ($z = 400$–800 m), with an increase from 1–1.5 to 2.5–3 m/s (*compare* red lines in Figure 7d). In the lower boundary layer, these velocities are however lower than in the earlier two-CP collision.

The enhanced velocities at higher levels ($z > 1{,}000$ m) are a consequence of the neutrally stratified atmosphere that allows any positive buoyancy perturbation—as, for example, the initial random perturbations—to rise indefinitely. This leads to increased high-level vertical velocities for the simulations with larger distance d (Figures 7c and 7d). In more realistic atmospheres with stable stratification above a neutrally stratified boundary layer, these updrafts are capped at the top of the boundary layer (*see* discussion below and Figure C1).

Note that the amplitude of vertical velocities shows high sensitivity to the numerical resolution—our simulations showing maximum vertical velocities at single CP gust fronts being a factor two higher for $\Delta x = 25$ m compared to $\Delta x = 100$ m. Consequently, the vertical velocities in collisions as reported in this section are expected to increase (decrease) with higher (lower) numerical resolution.

Upward transport of cold pool and surface air. In the triggering of convection not only the strength but also the height of the updrafts is important, both from a dynamic and thermodynamic perspective. The kinetic energy from strong updrafts at higher levels can help overcome stable layers that cap a boundary layer (Figure 9; Grandpeix & Lafore, 2010). From a thermodynamic perspective, convection is favored by a (gradual) moistening of the free-troposphere air when moist near-surface and boundary layer air is lifted above the lifting condensation level (LCL). Numerical and observational studies have identified a (gradual) premoistening of the midtroposphere (between 2 and 4 km) as an important process preceding the onset of heavy rainfall events and the transition from shallow to deep convection (Zhang & Klein, 2010). Specifically in the absence of large-scale advection of moist air masses, this moistening seems to be provided by local shallow convection. CPs may play an important role in accelerating this process by concentrating the moisture in the boundary layer, thereby clustering and widening the shallow convective clouds (Kurowski et al., 2018; Seifert & Heus, 2013; Schlemmer & Hohenegger, 2014). Little consideration however is usually given to the role of CPs in enhancing and spatially concentrating the moisture in the lower troposphere by increased mass flux along CP gust fronts. During CP collisions, these fronts become stationary and thus increase the moisture in a confined area for an extended period of time (Fuglestvedt & Haerter, 2020).

As a proxy for the moisture flux, we consider the accumulated vertical mass flux through the top of the boundary layer (here assumed to be at $z_{BL} = 1$ km)

$$\mathrm{MF}(x, y, z_{BL}) = \int_{t_0}^{t_1} \mathrm{d}t \rho(t, x, y, z_{BL}) w(t, x, y, z_{BL}),$$

where ρ is the density of air, $t_0 = 10$ min is the spin-up time and $t_1 = t_{3CP} + 15$ min (*compare* Figures 8a–8c). This mass flux is clearly enhanced along the two-CP collision lines and peaks above the three-CP collision point (Figure 8d). This enhancement can be understood as a result of the combined

effects of increased vertical velocities and the stationary location of the updraft fronts, which allows the updrafts to increase the moisture within a confined area over longer time.

Additionally, the CP height serves as an estimate of the height to which the near-surface air is transported. This is based on the assumption that during its propagation, the CP lifts the environmental air above its top (*compare* streamlines in Figure 1d). Throughout the single-CP time window ($t_0 \leq t < t_{2CP}$), the CP height remains roughly constant at about 200 m (Figure 8d, black curves). During the two-CP collision, the cold air is pushed to above 600 m (blue curves). Finally, in the three-CP collision, the air is pushed close to the boundary layer top at 1 km (red curves). By using passive tracers, initialized at the lowest model level, we verified that the CP height as measured above indeed gives a lower bound on the lifting level of near-surface air.

Stable Atmosphere. Similar analyses were conducted in simulations with stably stratified atmosphere (at $z \geq 1{,}000$ m). The CPs expand at slightly decreased speed, resulting in later collision times (Table C1). This resonates with theoretical findings of slower gravity current propagation speeds in channels of decreased depth (Benjamin, 1968; Moncrieff & So, 1989). In the boundary layer, the collisions lead to very similar results (Figure C1), differing only in that updrafts are somewhat shallower in the stable case ($z <$ 700 m vs. $z < 900$ m). Above the boundary layer ($z \geq 1{,}000$ m), the simulations differ strongly, as in the stable case the initial collapse of the cold air anomaly generates gravity waves that generate strong vertical velocities above the boundary layer. These waves are reinforced when the CPs collide and enhanced the mass flux locally.

5. Discussion and Conclusion

Our LES experiments represent highly simplified cold pool (CP) dynamics. This allows to isolate the dynamic effects of CPs from unsystematic perturbations in the CPs' surroundings, such as preexisting wind shear or variations in temperature and moisture. By removing such perturbations we can probe, how CP properties scale with the intensity and size of the rain cell that caused the CP's initial potential energy and compare updraft strength and mass flux that are generated in collisions of two and three CPs.

Insensitivity to initial cold pool geometry. To a good approximation, key dynamic features, such as CP propagation speed and the strength of convergence and updrafts ahead of the CP head, are unaffected by the geometry and temperature of the initial cold air anomaly, as long as the CP's initial potential energy is kept constant. This initial potential energy combines the spatial and (dry) thermodynamic parameters of CP initialization, which reduces the space of scaling parameters (Droegemeier & Wilhelmson, 1987) to a single extensive and conserved variable. Some sensitivity to the geometry of the initial perturbation can be observed in the CP volume and maximum vorticity in the CP head, in line with Droegemeier and Wilhelmson (1987). From a modeling perspective, the detected insensitivity to the initial geometry allows to generalize our results and compare them to studies that use different initialization configurations, such as cold bubbles that are released above the surface (Grant & van den Heever, 2016; Rooney, 2015).

In our simplified setup, moisture and microphysics are neglected. However, since potential energy is an extensive variable, it can be related to the amount of rain that is required to evaporate in order to cool the subcloud air column through latent heat uptake (*compare* Figure 5). To estimate how much rain has to evaporate to generate the CP's potential energy, we greatly simplify the small-scale details of microphysics (rain drop size distributions, presence of ice meteors, etc.) and convective turbulence by neglecting spatial and temporal variations in rain intensity and subcloud humidity, thus assuming constant evaporation rate. Furthermore, we approximate the entire rain volume to fall instantaneously, hence assuming that dissipation of CP potential energy is slow compared to the lifetime of the rain event. Under these assumptions, the sensitivity experiments presented in section 3.2 (Figure 4) indicate that precipitation intensity and cell size combined determine the strength of CPs. More comprehensive studies with moist CP dynamics will allow to verify these conclusions and test against similar findings from numerical studies, stating a linear relation between maximum precipitation intensity and the CP strength in terms of its radial velocity (Fournier & Haerter, 2019). The scaling of CP expansion with potential energy furthermore may assist a better understanding of the kinetics and internal vortical circulation of CPs, which play a crucial role in the mechanical forcing during CP collisions (Cafaro & Rooney, 2018) and are important factors for CP dissipation (Grant & van den Heever, 2016, 2018; Romps & Jeevanjee, 2016; Rooney, 2018).

The steady-state CP propagation speed U for inviscid, irrotational (i.e., internal motion is neglected) and incompressible gravity currents has been expressed as (Benjamin, 1968; von Karman, 1940)

$$U = \sqrt{2gH\frac{\rho'}{\rho}} \approx f(\mathrm{PE}_d).$$

This has been extended to gravity currents with non-zero internal motion by Moncrieff and So (1989). The potential energy density can be approximated as $\mathrm{PE}_d \approx g\rho' H$ (Benjamin, 1968), allowing to relate this expression to our scaling. However, such a steady-state solution requires a continuous forcing of the gravity current, provided by a constantly cooling source of PE in inflow experiments, and does not explain the decreasing CP propagation velocity with time (Benjamin, 1968; Droegemeier & Wilhelmson, 1985; Moncrieff & So, 1989). The power law scaling we propose (Equation 5) is more in line with the dynamics derived from similarity theory ($R \sim t^{1/2}$ Rooney, 2015) or vorticity conservation ($R \sim t^{2/3}$Rooney, 2018). The latter assumes that the vortical circulation in the CP head (*compare* Figure 3) is maintained and drives the CP propagation through its interaction with the surface. This seems to be a good prediction for the strong CPs ($r^* >$ 1,000 m) before the observed dynamic transition ($t < t_{\mathrm{trans}}$). We interpret the "kink" in scaling at the transition as an abrupt repartitioning of kinetic energy from a predominantly radial component to an additional strong azimuthal contribution by the onset of "lobe-and-cleft" instabilities. This could be seen as the activation of additional degrees of freedom at $t = t_{trans}$. We speculate that the lower exponent after the transition ($m_2 \approx 0.4 < 2/3$) originates from the quick decay of vorticity after the onset of instabilities.

Importance of cold pool collisions. Our results on CP collisions (section 4) can be summarized as follows: during two-CP collisions, strongest midboundary layer updrafts are generated where the two CPs meet. These updrafts are somewhat amplified if a third CP is present in the vicinity. During a three-CP collision, low-boundary layer updrafts are slightly weaker, most likely due to CP dissipation during their life cycle. However, updrafts in the upper boundary layer (400–900 m) are enhanced where the three CPs meet and cold CP air is forced much higher up (1,000 m). This implies, that moist near-surface air is mechanically lifted above the boundary layer and the lifting condensation level (LCL), where it either directly initiates a new convective event or contributes to preFimoistening as a crucial precursor for deep convection (Kurowski et al., 2018; Zhang & Klein, 2010). Accumulated vertical mass flux is a useful proxy for vertical moisture transport, combining updraft height and velocity. It is clearly enhanced by a factor two or more along collision lines, where the stationary updraft fronts confine the upward transport to a small area (Fuglestvedt & Haerter, 2020). By contrast, the updrafts ahead of an expanding single CP lead to a moderate flux that is distributed over a larger area and is compensated by the downward circulation in the interior of the CP.

In combination, updraft strength and mass flux show that differences between two- and three-CP collisions are smaller than between a single CP gust front and a two-CP collision. This suggests that parameterization schemes that aim at representing the effect of CPs on convection triggering, should distinguish between single CP gust fronts versus locations of multi-CP collisions (Figure 9b). The distinction between two- and three-CP collisions may however become important in strongly inhibited situations, where updrafts have to penetrate a layer of (conditionally) stable stratification near the top of the boundary layer. In such cases, the deeper updrafts in three-CP collisions may provide the required additional mechanical forcing (Grandpeix & Lafore, 2010, Figure 9a). The vicinity of preexisting lines of enhanced horizontal convergence, for example, from shallow convection cells or sea breezes, is expected to have a similar effect and may further enhance this difference (Purdom, 1976).

Sea breezes have also prompted investigations into collisions between asymmetric CPs (Cafaro & Rooney, 2018; Kingsmill & Crook, 2003; van der Wiel et al., 2017), where the buoyancy ratio between the colliding density currents is varied. Whereas no strong dependence of the maximum height reached by the collided gravity currents was found, the denser current did propagate underneath the less dense, leading to a slanted collision interface. Due to the evaporative cooling causing the CP, temperature and moisture anomalies are often negatively correlated so that the overrunning CP may be drier than the underlying one. This moisture stratification might then reduce the potential of cloud formation. This consideration implies that the origin of the density difference—the exact combination of temperature and moisture anomaly—may well play a role in determining, whether new updrafts can be formed under collision. The slanted collision interface furthermore brings with it that the collision line becomes nonstationary and moves with

the gust front of the upper density current. This may well reduce the locally accumulated mass flux, thereby decreasing the difference between a single CP gust front and CP collisions in terms of the vertical moisture transport. Presumably, a tilted collision plane may also alter the height of the generated updrafts. Such cases should be investigated in a future study, where moisture is explicitly taken into account.

A particular future challenge might be posed by the emergence of mesoscale convective systems (Houze Jr, 2004), which appear to hinge of the formation of "combined cold pools" (Haerter et al., 2020), formed by rapid successions of multi-CP interactions—finally leading to the formation of a joint, deeper CP. Through their large depth and potential energy, these CPs then act more autonomously, exciting subsequent updrafts near their periphery.

Altogether, the present study highlights the relevance of CP interactions. Our findings suggest, that the raincell—CP—raincell dynamics in populations of hundreds of raincells should be untangled and understood in terms of individual or multi-cold pool processes.

Appendix A: LES Initialization

A1. Initial Temperature Anomaly

The cold pools are initialized as temperature anomaly of radius r^* and height z^*, centered at x_c, y_c.

$$\begin{aligned} z_{max,0}(x,y) &= z^* \cdot \cos^2\left[\frac{\pi}{2}\frac{\sqrt{(x-x_c)^2+(y-y_c)^2}}{r^*}\right] \\ &= z^* \cdot \cos^2\left[\frac{\pi}{2}\frac{r}{r^*}\right] = z_{max,0}(r), \\ z_{max,\delta}(x,y) &= (z^*+\delta) \cdot \cos^2\left[\frac{\pi}{2}\frac{\sqrt{(x-x_c)^2+(y-y_c)^2}}{r^*+\delta}\right] \\ &= (z^*+\delta) \cdot \cos^2\left[\frac{\pi}{2}\frac{r}{r^*+\delta}\right] = z_{max,\delta}(r), \end{aligned}$$

The $\cos^2$ envelope is chosen based on its positivity and symmetry with regard to 0.

A2. Potential Energy

The potential energy of a volume V_{CP} of cold air, as initializing the CPs, is computed as

$$PE = g\int \frac{\theta'(\vec{x})}{\theta_0(z)}\rho_d(z)z\,dV, \tag{A1}$$

with θ' being the potential temperature anomaly, defined as the deviation from the horizontal domain mean potential temperature $\theta_0(z)$, and $\rho_d(z)$ the reference density profile.

In the simulations presented in this study, the temperature anomaly $\theta'(\vec{x})$ is constant within the volume V_{CP} and, due to the small volume covered by the CP ($V_{CP} \ll L_x L_y H$), approximately 0 in the environment ($\theta(\vec{x}) \approx \theta_0(z)$ for $\vec{x} \notin V_{CP}$). The relatively shallow anomalies ($z^* \leq 1{,}000$ m) furthermore allow to assume constant density $\rho_d(z) \approx \rho_0$ for the levels up to the CP top ($z \leq z^*$), allowing for the following simplifications

$$\mathrm{PE} \approx g\frac{\theta'}{\theta_0}\rho_0\int_{V_{CP}} z\,dV.$$

Transforming to cylindrical coordinates and using the expression for the envelope z_{max} defined in Equation A0.1, finally renders the following result

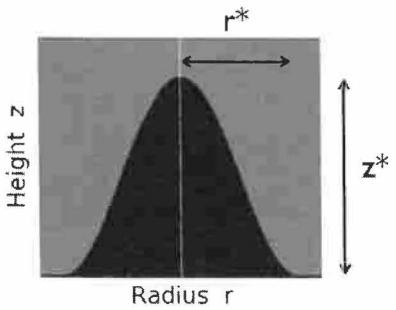

Figure A1. Initial configuration of cold pools in terms of a cold air "mountain" of height z^* and base radius r^*.

Table C1
Collision Times for the Two Sets of 3CP Simulations With Neutral and Stable Background Atmospheric Profile ($\theta' = 5$ K, $z^* = 1$ km, $r^* = 1.1$ km)

Separation d	Neutral t_{3CP}	Neutral t_{2CP}	Stable t_{2CP}	Stable t_{3CP}
10 km	1,100 s	1,500 s	1,100 s	1,500 s
12 km	1,500 s	2,200 s	1,600 s	2,300 s
15 km	2,400 s	3,300 s	2,500 s	3,600 s

$$\begin{aligned} \mathrm{PE} &\approx g\frac{\theta'}{\theta_0}\rho_0 2\pi \int_0^{r^*}\int_0^{z_{max}(r)} rz\,\mathrm{d}z\,\mathrm{d}r \\ &= 2\pi\ g\frac{\theta'}{\theta_0}\rho_0 \int_0^{r^*} r\frac{z_{max}(r)^2}{2}\mathrm{d}r, \\ &= \pi\ g\frac{\theta'}{\theta_0}\rho_0 \int_0^{r^*} r z_*^2 \cos^2\left[\frac{\pi}{2}\frac{r}{r_*}\right]\ \mathrm{d}r \\ &= \pi\, g\frac{\theta'}{\theta_0}\rho_0 (r_* z_*)^2 \left(\frac{1}{4} - \frac{1}{\pi^2}\right). \end{aligned}$$

leading to the following proportionality with respect to the CP temperature and geometry parameters that are varied in the simulations

$$\mathrm{PE} \propto \theta' (r_* z_*)^2. \tag{A2}$$

The *reference simulation* ($r^* = z^* = 1km, \theta' = 3K$) has an initial potential energy of $\mathrm{PE}_0 = 4.4 \cdot 10^7 kJ$.

Appendix B: Rain Intensities

The relation between rain intensity and initial PE of the CPs is approximated by computing how much energy needs to be extracted in order to cool the initial CP volume (i.e., the three-dimensional volumes enclosed by the envelopes sketched in Figure 5a) by a temperature drop θ'. Using an evaporation rate typical

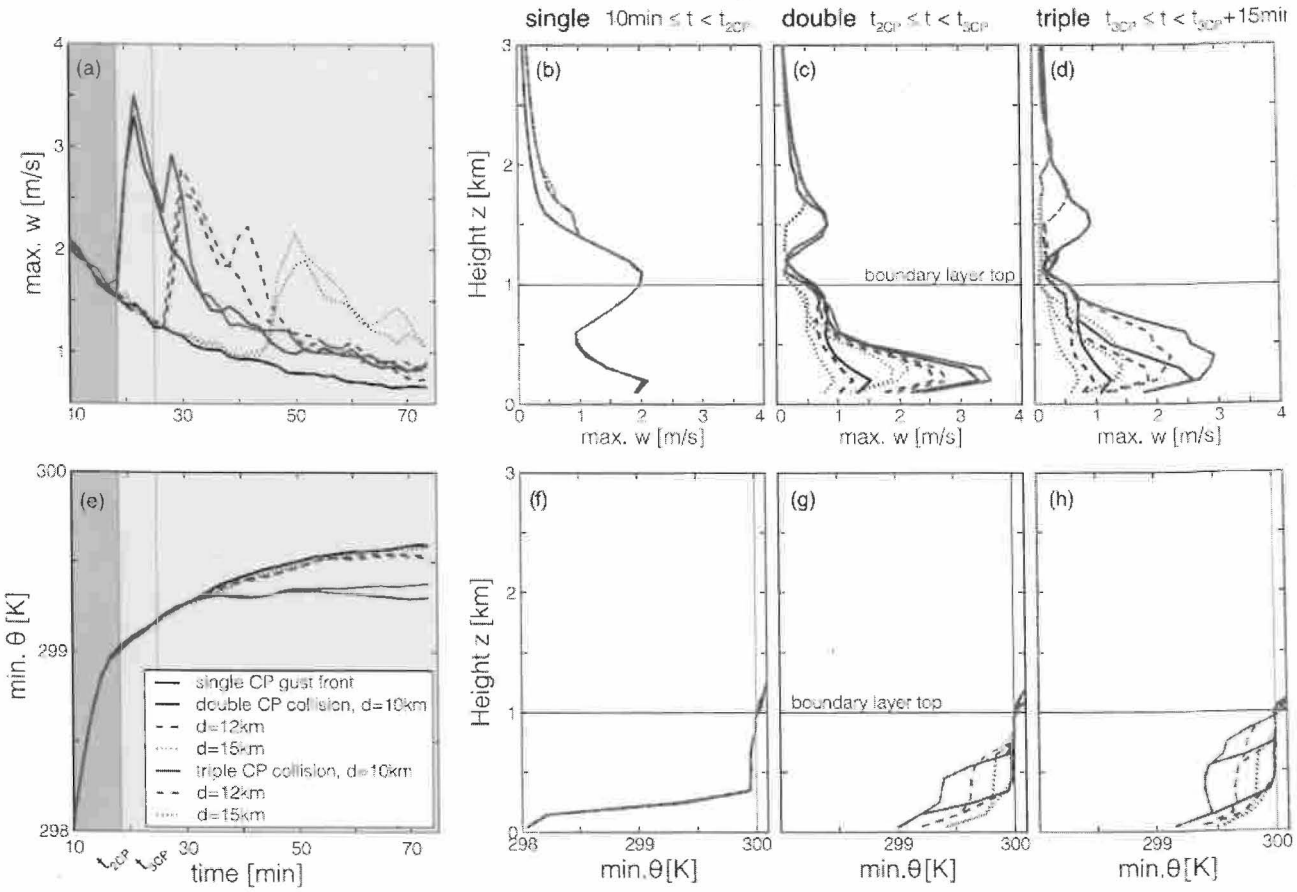

Figure C1. Same as in Figure 7 but with stably stratified background.

Table C2
Domain Size for the Simulations Used for the Collision Study in Section 4

Separation d	Single $L_{x,y}$ (km)	Double L_x (km)	Double L_y (km)	Triple $L_{x,y}$ (km)
—	32	—	—	—
10	—	48	36	40
12	—	80	40	60
15	—	80	40	80

Note. All simulations are run with CP parameters $\theta' = -5$ K, $z^* = 1$ km, $r^* = 1.1$ km at resolution $\Delta x = \Delta y = \Delta z = 100$ m.

for tropical convection of $\eta = 20\%$ (Worden et al., 2007) and assuming an area and duration of the rain event, this energy can then be converted into a rain intensity. For simplicity, the area and duration of the rain events are assumed to be the same for all CPs, allowing only the intensity to vary.

A rain cell area equal to the initial area of the reference CP ($A = \pi(r_0^*)^2 \approx 3$ km^2) and a duration $\tau = 30$ min is chosen (*note:* since the initial anomaly is $\cos^2$ shaped, one could also use a mean width of this "mountain" for r^*, reducing the area A and thus increasing the intensity I).

To cool a volume

$$V_{CP} = \int_0^{r^*} \mathrm{d}r \int_0^{z(r)} \mathrm{d}z = 2\pi (r^*)^2 z^* \left(\frac{1}{4} - \frac{1}{\pi^2}\right) \approx \pi/2 (r^*)^2 z^*$$

by $T' = T'(\theta' = 3K)$, an amount Q of energy needs to be extracted

$$Q = c_{p,d} \int_{V_{CP}} \mathrm{d}V\, T'(\theta', p(z)) \cdot \rho_d(z).$$

This energy Q can be related to the latent heat absorbed when an amount of $m_w = Q/L_v$ water evaporates, where $L_v \approx$ 2,500 kJ/kg is the specific latent heat of water at an ambient temperature of 0°C (Srivastava, 1985). We now assume that this water results from rain evaporated at a rate η in the sub-cloud layer below a rain cell of area A, which rains during a time τ at an intensity I

$$I = m_w/(\eta \rho_w \tau A),$$

where $\rho_w = 1{,}000\ \mathrm{kg\ m^{-3}}$ is the liquid water density.

Appendix C: Cold Pool Collisions

Data Availability Statement

The PyCLES code used for the cold pool simulations is accessible at this site (https://github.com/pressel/pycles). The initial configuration and namelist files will be made available upon publication. The cold pool tracking code used for measuring the cold pool radius is described in Henneberg et al. (2020) and available online (http://doi.org/10.5281/zenodo.3665813).

Acknowledgments
The authors gratefully acknowledge funding by a grant from the VILLUM Foundation (grant number: 13168) and the European Research Council (ERC) under the European Union's Horizon 2020 research and innovation program (grant number: 771859). The authors acknowledge the Danish Climate Computing Center (DC3) and Roman Nuterman for technical support.

References

Addis, R. P., Garstang, M., & Emmitt, G. D. (1984). Downdrafts from tropical oceanic cumuli. *Boundary-Layer Meteorology, 28*, 23–49. https://doi.org/10.1007/BF00119455

Benjamin, T. B. (1968). Gravity currents and related phenomena. *Journal of Fluid Mechanics, 2*, 109–248. https://doi.org/10.1017/S0022112068000133

Cafaro, C., & Rooney, G. G. (2018). Characteristics of colliding density currents: A numerical and theoretical study. *Quarterly Journal of the Royal Meteorological Society, 144*(715), 1761–1771. https://doi.org/10.1002/qj.3337

Drager, A. J., & van den Heever, S. C. (2017). Characterizing convective cold pools. *Journal of Advances in Modeling Earth Systems, 9*, 1091–1115. https://doi.org/10.1002/2016MS000788

Droegemeier, K., & Wilhelmson, R. (1985). Three-dimensional numerical modeling of convection produced by interacting thunderstorm outflows. Part I: Control simulation and low-level moisture variations. *Journal of the Atmospheric Sciences, 42*(22), 2381–2403. https://doi.org/10.1175/1520-0469(1985)042<2381:TDNMOC>2.0.CO;2

Droegemeier, K., & Wilhelmson, R. (1987). Numerical simulation of thunderstorm outflow dynamics. Part I: Outflow sensitivity experiments and turbulence dynamics. *Journal of the Atmospheric Sciences, 44*(8), 1180–1210. https://doi.org/10.1175/1520-0469(1987)044<1180:NSOTOD>2.0.CO;2

Feng, Z., Hagos, S., Rowe, A. K., Burleyson, C. D., Martini, M. N., & de Szoeke, S. P. (2015). Mechanisms of convective cloud organization by cold pools over tropical warm ocean during the AMIE/DYNAMO field campaign. *Journal of Advances in Modeling Earth Systems, 7*, 357–381. https://doi.org/10.1002/2014MS000384

Fournier, M., & Haerter, J. O. (2019). Tracking the gust fronts of convective cold pools. *Journal of Geophysical Research: Atmospheres, 124*, 11,103–11,117. https://doi.org/10.1029/2019JD030980

Fuglestvedt, H. F., & Haerter, J. O. (2020). Cold pools as conveyor belts of moisture. *Geophysical Research Letters, 47*, e2020GL087319. https://doi.org/10.1029/2020GL087319

Goff, R. C. (1975). Thunderstorm-outflow kinematics and dynamics. NOAA Technical Memorandum ERL NSSL-75. Retrieved from https://repository.library.noaa.gov/view/noaa/17627
Grandpeix, J.-Y., & Lafore, J.-P. (2010). A density current parameterization coupled with Emanuel's convection scheme. Part i: The models. *Journal of the Atmospheric Sciences*, *67*, 881–897. https://doi.org/10.1175/2009JAS3044.1
Grant, L. D., & van den Heever, S. C. (2016). Cold pool dissipation. *Journal of Geophysical Research: Atmospheres*, *121*, 1138–1155. https://doi.org/10.1002/2015JD023813
Grant, L. D., & van den Heever, S. C. (2018). Cold pool-land surface interactions in a dry continental environment. *Journal of Advances in Modeling Earth Systems*, *10*, 1513–1526. https://doi.org/10.1029/2018MS001323
Haerter, J. O., Berg, P., & Moseley, C. (2017). Precipitation onset as the temporal reference in convective self-organization. *Geophysical Research Letters*, *44*, 6450–6459. https://doi.org/10.1002/2017GL073342
Haerter, J. O., Böing, S. J., Henneberg, O., & Nissen, S. B. (2019). Circling in on convective organization. *Geophysical Research Letters*, *46*, 7024–7034. https://doi.org/10.1002/2017GL073342
Haerter, J. O., Meyer, B., & Nissen, S. B. (2020). Diurnal self-aggregation. *npj Climate and Atmospheric Science*, *3*, 30. https://doi.org/10.1038/s41612-020-00132-z
Härtel, C., Carlsson, F., & Thunblom, M. (2000). Analysis and direct numerical simulation of the flow at a gravity-current head. Part 2. The lobe-and-cleft instability. *Journal of Fluid Mechanics*, *418*, 213–229. https://doi.org/10.1017/S0022112000001270
Henneberg, O., Meyer, B., & Haerter, J. O. (2020). Particle-based tracking of cold pool gust fronts. *Journal of Advances in Modeling Earth Systems*, *11*, e2019MS001910. https://doi.org/10.1029/2019MS001910
Hirt, M., Craig, G. C., Schäfer, S. A. K., Savre, J., & Heinze, R. (2020). Cold pool driven convective initiation: Using causal graph analysis to determine what convection permitting models are missing. *Quarterly Journal of the Royal Meteorological Society*, *146*, 2205–2227. https://doi.org/10.1002/qj.3788
Houze Jr, R. A. (2004). Mesoscale convective systems. *Reviews of Geophysics*, *42*, RG4003. https://doi.org/10.1029/2004RG000150
Johnson, R. H., & Nicholls, M. E. (1983). A composite analysis of the boundary layer accompanying a tropical squall line. *Monthly Weather Review*, *111*, 308–319.
Kingsmill, D. E., & Crook, N. A. (2003). An observational study of atmospheric bore formation from colliding density currents. *Monthly Weather Review*, *131*(12), 2985–3002.
Kneller, B. C., Bennett, S. C., & McCaffrey, W. D. (1999). Velocity structure, turbulence and fluid stresses in experimental gravity currents. *Journal of Geophysical Research*, *104*(C3), 5381–5391. https://doi.org/10.1029/1998JC900077
Kurowski, M. J., Suselj, K., Grabowski, W. W., & Teixeira, J. (2018). Shallow-to-deep transition of continental moist convection: Cold pools, surface fluxes, and mesoscale organization. *Journal of the Atmospheric Sciences*, *75*(12), 4071–4090. https://doi.org/10.1175/JAS-D-18-0031.1
Langhans, W., & Romps, D. M. (2015). The origin of water vapor rings in tropical oceanic cold pools. *Geophysical Research Letters*, *42*, 7825–7834. https://doi.org/10.1002/2015GL065623
Leutwyler, D., Fuhrer, O., Lapillonne, X., Lüthi, D., & Schär, C. (2016). Towards European-scale convection-resolving climate simulations with GPUs: A study with COSMO 4.19. *Geoscientific Model Development*, *9*(9), 3393–3412. https://doi.org/10.5194/gmd-9-3393-2016
Markowski, P., & Richardson, Y. (2010). *Mesoscale meteorology in midlatitudes*. Penn State University, University Park, PA, USA: John Wiley and Sons. https://doi.org/10.1002/9780470682104
Moncrieff, M. W., & Liu, C. (1999). Convection initiation by density currents: Role of convergence, shear, and dynamical organization. *Monthly Weather Review*, *127*, 2455–2464.
Moncrieff, M. W., & So, D. W. K. (1989). A hydrodynamical theory of conservative bounded density currents. *Journal of Fluid Mechanics*, *198*(Moncrieff, M., & So, D.), 177–197. https://doi.org/10.1017/S0022112089000091
Nissen, S. B., & Haerter, J. O. (2020). Self-aggregation conceptualized by cold pool organization. arXiv:1311.12849v2.
Parsons, D., Dabberdt, W., Cole, H., Hock, T., Martin, C., Barrett, A.-L., et al. (1994). The integrated sounding system: Description and preliminary observations from TOGA COARE. *Bulletin of the American Meteorological Society*, *75*(4), 553–567.
Pressel, K. G., Kaul, C. M., Schneider, T., Tan, Z., & Mishra, S. (2015). Large-eddy simulation in an anelastic framework with closed water and entropy balances. *Journal of Advances in Modeling Earth Systems*, *7*, 1425–1456. https://doi.org/10.1002/2015MS000496
Purdom, J. F. W. (1976). Some uses of high-resolution goes Imagery in the mesoscale forecasting of convection and its behavior. *Monthly Weather Review*, *104*, 1474–1483. https://doi.org/10.1175/1520-0493(1976)104<1474:SUOHRG>2.0.CO;2
Romps, D. M., & Jeevanjee, N. (2016). On the sizes and lifetimes of cold pools. *Quarterly Journal of the Royal Meteorological Society*, *142*, 1517–1527. https://doi.org/10.1002/qj.2754
Rooney, G. G. (2015). Descent and spread of negatively buoyant thermals. *Journal of Fluid Mechanics*, *780*, 457–479. https://doi.org/10.1017/jfm.2015.484
Rooney, G. G. (2018). Similarity-based approximations for the evolution of a gravity current. *Quarterly Journal of the Royal Meteorological Society*, *144*(716), 2302–2310. https://doi.org/10.1002/qj.3371
Rotunno, R., Klemp, J. B., & Weisman, M. L. (1988). A theory for strong, long-lived squall lines. *Journal of the Atmospheric Sciences*, *45*(3), 463–485. https://doi.org/10.1175/1520-0469(1988)045<0463:ATFSLL>2.0.CO;2
Schlemmer, L., & Hohenegger, C. (2014). The formation of wider and deeper clouds as a result of cold-pool dynamics. *Journal of the Atmospheric Sciences*, *71*, 2842–2858. https://doi.org/10.1175/JAS-D-13-0170.1
Seifert, A., & Heus, T. (2013). Large-eddy simulation o organized precipitating trade wind cumulus clouds. *Atmospheric Chemistry and Physics*, *13*, 5631–5645. https://doi.org/10.5194/acp-13-5631-2013
Simpson, J. E. (1972). Effects of the lower boundary on the head of a gravity current. *Journal of Fluid Mechanics*, *53*, 759–768. https://doi.org/10.1017/S0022112072000461
Simpson, J. (1980). Downdrafts as linkages in dynamic cumulus seeding effects. *Journal of Applied Meteorology*, *19*(4), 477–487. https://doi.org/10.1175/1520-0450(1980)019<0477:DALIDC>2.0.CO;2
Smagorinsky, J. (1963). General circulation experiments with the primitve equations. *Monthly Weather Review*, *91*(3), 99–164. https://doi.org/10.1175/1520-0493(1963)091<0099:GCEWTP>2.3.CO;2
Srivastava, R. C. (1985). A simple model of evaporatively driven downdraft: Application to microburst downdraft. *Journal of the Atmospheric Sciences*, *42*(10), 1004–1023. https://doi.org/10.1175/1520-0469(1985)042<1004:ASMOED>2.0.CO;2
Tompkins, A. M. (2001a). Organization of tropical convection in low vertical wind shears: The role of water vapor. *Journal of the Atmospheric Sciences*, *58*, 529–545. https://doi.org/10.1175/1520-0469(2001)058<0529:OOTCIL>2.0.CO;2
Tompkins, A. M. (2001b). Organization of tropical convection in low vertical wind shears: The role of cold pools. *Journal of the Atmospheric Sciences*, *58*, 1650–1672. https://doi.org/10.1175/1520-0469(2001)058<1650OOTCIL>2.0CO;2

Torri, G., & Kuang, Z. (2019). On cold pool collisions in tropical boundary layers Giuseppe. *Geophysical Research Letters*, *46*, 399–407. https://doi.org/10.1029/2018GL080501

Torri, G., Kuang, Z., & Tian, Y. (2015). Mechanisms for convection triggering by cold pools. *Geophysical Research Letters*, *42*, 1943–1950. https://doi.org/10.1002/2015GL063227

van der Wiel, K., Gille, S. T., Llewellyn Smith, S. G., Linden, P. F., & Cenedese, C. (2017). Characteristics of colliding sea breeze gravity current fronts: A laboratory study. *Quarterly Journal of the Royal Meteorological Society*, *143*(704), 1434–1441.

von Karman, T. (1940). The engineer grapples with nonlinear problems. *Bulletin American Meteorological Society*, *46*, 615–683. https://doi.org/10.1090/S0002-9904-1940-07266-0

Wakimoto, R. (2001). Convectively driven high wind events. In C. A. Doswell (Ed.), *Severe convective storms* (pp. 255–298). Boston, MA: Meteorological Monographs. American Meteorological Society.

Worden, J., Noone, D., Bowman, K., Beer, R., Eldering, A., Fisher, B., et al. (2007). Importance of rain evaporation and continental convection in the tropical water cycle. *Nature*, *445*(7127), 528–532. https://doi.org/10.1038/nature05508

Zhang, Y., & Klein, S. A. (2010). Mechanisms affecting the transition from shallow to deep convection over land: Inferences from observations of the diurnal cycle collected at the arm southern great plains site. *Journal of the Atmospheric Sciences*, *67*, 2943–2959. https://doi.org/10.1175/2010JAS3366.1

Zuidema, P., Torri, G., Muller, C., & Chandra, A. (2017). A survey of precipitation-induced atmospheric cold pools over oceans and their interactions with the larger-scale environment. *Surveys in Geophysics*, *38*(6), 1283–1305. https://doi.org/10.1007/s10712-017-9447-x